UC Berkeley
UC Berkeley Previously Published Works

Title

Latched detection of zeptojoule spin echoes with a kinetic inductance parametric oscillator

Permalink

Journal

ISSN

Authors

Vine, Wyatt
Kringhøj, Anders
Savytskyi, Mykhailo
et al.

Publication Date

DOI

Peer reviewed

Latched detection of zeptojoule spin echoes with a kinetic inductance parametric oscillator

Wyatt Vine[1], Anders Kringhøj[1], Mykhailo Savytskyi[1], Daniel Parker[1], Thomas Schenkel[2], Brett C. Johnson[3], Jeffrey C. McCallum[4], Andrea Morello[1], Jarryd J. Pla[1]*

When strongly pumped at twice their resonant frequency, nonlinear resonators develop a high-amplitude intracavity field, a phenomenon known as parametric self-oscillations. The boundary over which this instability occurs can be extremely sharp and thereby presents an opportunity for realizing a detector. Here, we operate such a device based on a superconducting microwave resonator whose nonlinearity is engineered from kinetic inductance. The device indicates the absorption of low-power microwave wavepackets by transitioning to a self-oscillating state. Using calibrated pulses, we measure the detection efficiency to zeptojoule energy wavepackets. We then apply it to measurements of electron spin resonance, using an ensemble of [209]Bi donors in silicon that are inductively coupled to the resonator. We achieve a latched readout of the spin signal with an amplitude that is five hundred times greater than the underlying spin echoes.

INTRODUCTION

Over the past decade, quantum-limited parametric amplifiers operating at microwave frequencies have progressed from proof of principle to ubiquity within circuit quantum electrodynamics (cQED) experiments. Typically, these devices are operated in a linear regime, but several types of parametric amplifiers are explicitly nonlinear, such as the Josephson bifurcation amplifier (JBA) (*1*) and the Josephson parametric oscillator (JPO) (*2*–*4*). These devices essentially act as a microwave "click" detector, in that threshold detection is used to discriminate the presence or absence of a signal. Central to the design of JBAs and JPOs is the use of Josephson junctions, which provide the nonlinearity required for signal mixing. An alternative source of nonlinearity is the kinetic inductance intrinsic to thin films of disordered superconductors (*5*). In contrast to Josephson junction–based devices, superconducting microwave resonators engineered from high kinetic inductance materials retain high-quality factors when operated in tesla-strength magnetic fields (*6*, *7*) and at elevated temperatures (*8*). This has recently inspired the development of magnetic field-compatible resonant parametric amplifiers that operate close to the quantum noise limit (*8*–*12*), which have a range of applications including axion detection (*13*) and quantum computation with spin qubits (*14*).

Another application of these devices is the measurement of electron spin resonance (ESR). JPAs have already been used to push noise in ESR experiments to the quantum limit, where vacuum fluctuations of the electromagnetic field dictate the spin detection sensitivity (*15*, *16*). Several other recent works have applied nonlinear microwave amplifiers (*17*) and qubit-based sensors (*18*–*21*) using Josephson junctions to measurements of ESR to push detection sensitivities to record levels. Kinetic inductance parametric amplifiers (KIPAs) have also recently been used for ESR, where they have been demonstrated to have several advantages over JPAs (*12*). Because of their compatibility with moderate magnetic fields, KIPAs can serve

as both the resonator for inductive detection of spin echo signals and the first-stage amplifier. This not only simplifies the measurement setup by obviating a separate quantum-limited amplifier, it also eliminates any insertion loss between the resonator and the first cryogenic amplifier.

Here, we extend previous works with KIPAs by operating one as a click detector rather than as a linear amplifier. By biasing the device near the threshold where its behavior transitions from a linear amplifier to a parametric oscillator, the onset of parametric self-oscillations (PSO) serves as a binary indicator for the absorption of microwave wavepackets. To distinguish this operating regime, which has not been previously demonstrated, we refer to the device here as a kinetic inductance parametric oscillator (KIPO), in analogy to the JPO which operates under a similar principle. In the following, we describe the concept of the detector, calibrate its sensitivity, and demonstrate its application in ESR measurements of an ensemble of bismuth ([209]Bi) donors in silicon (Si) that are directly coupled to the device.

Results

Device design

Our device is similar to the KIPAs described in previous works (*9*, *12*). It is patterned in a single lithographic step from a 50-nm-thick film of niobium titanium nitride (NbTiN) with a kinetic inductance of $L_k = 3.45$ pH/□. The NbTiN is deposited on a Si substrate enriched in the isotope [28]Si [750 parts per million (ppm) residual [29]Si] that was implanted with [209]Bi donors at a concentration of 10^{17} cm^{-3} over a depth of 1.35 μm. The device has a single port and consists of a quarter-wavelength (λ/4) coplanar waveguide resonator that is shorted to ground at one end and galvanically connected to a band-stop stepped impedance filter (BS-SIF) (*22*) at the other end (Fig. 1, A and B). The resonator features a dense interdigitated capacitor with 1-μm-wide fingers and a 1.5-μm gap to ground (see the Supplementary Materials), which compensates for the strong kinetic inductance and reduces the impedance of the mode to $Z_0 \approx 33$ ohm. The BS-SIF serves to confine the resonant mode of the device while simultaneously allowing the application of a DC bias current (I_{DC}). An I_{DC} can be used to tune the resonance frequency from $\omega_0(I_{DC} = 0)/2\pi = 7.776$ GHz to

[1]School of Electrical Engineering and Telecommunications, UNSW Sydney, Sydney, New South Wales 2052, Australia. [2]Accelerator Technology and Applied Physics Division, Lawrence Berkeley National Laboratory, Berkeley, CA 94720, USA. [3]School of Science, RMIT University, Melbourne, Victoria 3001, Australia. [4]School of Physics, University of Melbourne, Parkville, Victoria 3010, Australia.
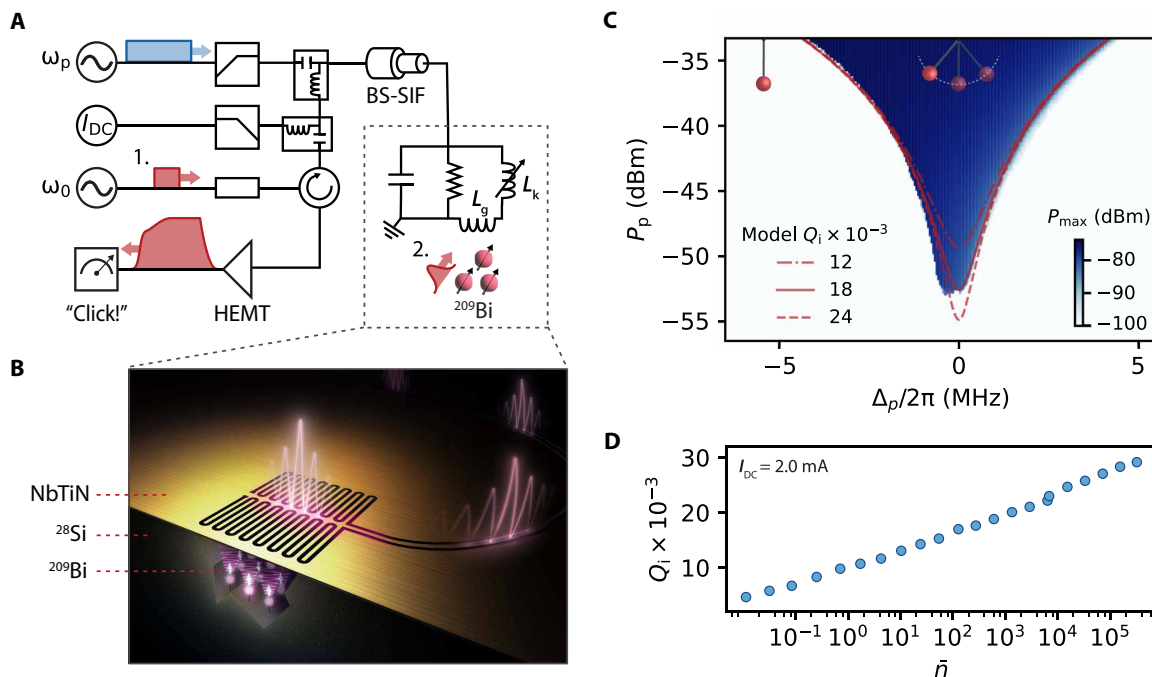*Corresponding author. Email: jarryd@unsw.edu.au

Fig. 1. Measurement schematic and device characterization. (**A**) The device is represented by a parallel RLC resonator with frequency ω_0 and a BS-SIF. The resonator has a geometric inductance (L_g) and a kinetic inductance (L_k). We operate the device as a click detector by biasing it with a strong pump with frequency ω_p and a DC current I_{DC}. In this work, we detect two types of signals: weak classical signals with frequency near ω_0 generated by a microwave source (1), which we use to calibrate the detector's sensitivity, and spin echoes from an ensemble of ^{209}Bi donor spins (2) that are resonantly coupled to the resonator via L_g. Detailed schematics of the measurement setups are presented in the Supplementary Materials. (**B**) An artist's depiction of the resonator, which is formed from a $\lambda/4$ section of transmission line with a dense interdigitated capacitor. ^{209}Bi spins are implanted into the silicon substrate. (**C**) The maximum power measured with a spectrum analyzer centered at ω_0 as a function of $\Delta_p = \omega_p - 2\omega_0$ and the pump power P_p. The dark blue region corresponds to the parameter space where the device self-oscillates. The powers are referred to the output of the device, and P_{max} is truncated at -100 dBm to enhance clarity. The red lines correspond to the PSO threshold (P_{th}) predicted from a model of the device using three different values of Q_i. The stationary and swinging pendulums are used to depict the quiet and self-oscillating states of the device, respectively. (**D**) Q_i extracted from measurements of S_{11} performed with a VNA as the signal power is varied. Measurements were taken at $T = 10$ mK.

$\omega_0(I_{DC} = 4.89 \text{ mA})/2\pi = 7.530$ GHz via the quadratic dependence of L_k on the total current (*23*). An I_{DC} also enables three-wave mixing so that a pump with frequency $\omega_p \approx 2\omega_0$ can be used to amplify signals with frequencies about ω_0 (*9*, *24*). The device is connected to the cold finger of a dilution refrigerator with a base temperature of 10 mK or a pumped ^{3}He cryostat with a base temperature of 400 mK, depending on the experiment. The DC current and microwave tones are combined at base temperature using a bias tee and diplexer (Fig. 1A). The device is measured in reflection with the signal being routed through a cryogenic high electron mobility transistor (HEMT) amplifier at 4 K. Further details of the device design and measurement setup are provided in the Supplementary Materials.

Detector concept

The defining characteristic of PSO is the formation of a large intracavity field at ω_0 whenever the three-wave mixing strength exceeds the average rate at which resonant photons can escape the cavity. Experimentally, this manifests as the sudden generation of a large power at ω_0 that is emitted from the device whenever the pump power P_p is raised beyond a sharp threshold P_{th}. In Fig. 1C, we report the maximum power recorded by a spectrum analyzer (P_{max}) centered at ω_0 as a function of P_p and a detuning of the pump frequency $\Delta_p = \omega_p - 2\omega_0$. The dark blue region corresponds to the parameter space where the

device undergoes PSO, and the boundary of this region provides a direct measurement of P_{th}.

Using cavity input-output theory and the Hamiltonian for the KIPA (*9*), we model our device as a parametrically driven Duffing oscillator (see the Supplementary Materials), as has been done previously for JPOs (*2*, *25*, *26*). Using parameters extracted from measurements of the device, we directly compare the model and our experimental measurement of the threshold power P_{th} (red lines in Fig. 1C). Crucially, the model predicts that when $\Delta_p = 0$, $P_{th} \propto (Q_i^{-1} + Q_c^{-1})^2$, where Q_i and Q_c are the internal and coupling quality factors of the resonant mode, respectively. In Fig. 1C, we compare three models of the device which are equivalent except for Q_i. For this particular measurement, we find that there is reasonable agreement between the data and model for $Q_i = 18 \times 10^3$. We also highlight that P_{th} shifts to smaller values as Q_i is increased.

The quality factors Q_i and Q_c can be extracted from measurements of the device in reflection (S_{11}) using a vector network analyzer (VNA). As is common for superconducting microwave resonators, we observe that Q_i is nonlinear with the applied signal power, or equivalently, the average number of intracavity photons $\bar{n}$ (Fig. 1D). This indicates that two-level systems (TLSs) interact with the resonant mode (*27*) and limit Q_i at low signal power. We observe Q_i to vary between 4.7×10^3 and 29×10^3 for $10^{-2} < \bar{n} < 3 \times 10^5$, which, in all

cases, is much smaller than $Q_c \approx 200 \times 10^3$ (see the Supplementary Materials). An important consequence of this is that the resonant mode's linewidth $\omega_0(Q_i^{-1} + Q_c^{-1})$ and hence P_{th} are sensitive to the signal power inside the resonator.

The experiments shown in Fig. 2 demonstrate how the dependence of P_{th} on $\bar{n}$ can be used to create a device that detects the absorption of low-power microwave wavepackets. First, the device is biased with a DC current $I_{DC} = 2.55$ mA and a pump tone with frequency $\omega_p = 2\omega_0$. Following a delay $\tau_0 = 1$ ms, a stimulus pulse with duration $\tau_1 = 10$ μs, frequency ω_0, and power $P_0 = -116.4$ dBm is delivered to the input of the device (Fig. 2A). Throughout the experiment, we monitor the device by performing a homodyne measurement (i.e., demodulating the signal using a local oscillator with frequency $\omega_{LO} = \omega_0$) and recording the amplitude of the signal quadrature components X and Y. For the lowest pump power P_p (Fig. 2B, iii), we observe no PSO. For the largest P_p (Fig. 2B, i), we observe PSO but at a time that is uncorrelated with the stimulus pulse. But for an appropriately chosen $P_p \approx P_{th}$ (Fig. 2B, ii), we observe the PSO onset at a time that is correlated with the stimulus pulse (the quiet and self-oscillating states are represented schematically with the pendulum). We hypothesize that absorption of the stimulus pulse triggers the onset of PSO due to the partial saturation of the TLSs; the increased Q_i associated with this results in P_{th} being dynamically reduced below the P_p setpoint, thereby triggering PSO.

From Fig. 2B, it is clear that the self-oscillating state has a large amplitude (α), relative to the stimulus pulse. Fig. 1C shows that the peak power of PSO can exceed -75 dBm. This can be understood by noting that $\alpha \propto 1/K$ for a Duffing oscillator, where K is the self-Kerr

strength (see the Supplementary Materials). The Kerr effect for these devices is known to be negligible relative to Josephson junction–based devices, due to the weak and distributed nature of the kinetic inductance nonlinearity [9]. Notably, α is independent of the stimulus power, so that the onset of PSO functions as a binary indicator for the pulse absorption. By comparing the power of PSO measured with a spectrum analyzer to the average number of intracavity photons $\bar{n}$ calculated from VNA measurements of S_{11} with a known power, we estimate that $\bar{n} > 10^5$ during PSO. For this device, α is large enough to enable subsequent four-wave mixing processes, which results in the generation of a frequency comb about ω_0 whenever the device self-oscillates (see the Supplementary Materials). This results in oscillations in the amplitude of the demodulated signal when the device is self-oscillating (Fig. 2B).

Detection efficiency and sensitivity

To calibrate the sensitivity of the detector, we measure its response using two pulse sequences. The first is depicted in Fig. 3A and is identical to that used in the previous section (Fig. 2A) but with different timings τ_0, τ_1, and τ_2. The second sequence is similar, differing only in that the stimulus pulse is omitted (Fig. 3B). Using threshold detection, this allows us to measure the efficiency of the sensor, $E = P(T|S) - P(T|\tilde{S})$, where T indicates that the device self-oscillates and S ($\tilde{S}$) indicates that the device receives (does not receive) a stimulus pulse. $P(T|S)$ is therefore the conditional probability describing the successful detection of the stimulus, and $P(T|\tilde{S})$ is the probability of observing a dark count.

In Fig. 3C, we measure the detection efficiency E as a function of the pump power P_p with a DC current $I_{DC} = 2.0$ mA, stimulus pulse duration $\tau_1 = 10$ μs, and stimulus pulse powers P_0 in the range $[-137, -111]$ dBm. We note that the gain of a linear parametric amplifier ($P_p < P_{th}$) operated in degenerate mode ($\omega_p = 2\omega_0$) is dependent on the relative phase between the pump and the signal [9]. For the present experiments, the relative phase between the stimulus pulse and the pump (ϕ_p) might therefore modulate E and require precise calibration. To circumvent this, we phase modulate the pump microwave source at a rate of 15 kHz. While the modulation rate is slower than $1/\tau_1 = 100$ kHz, for each data point, we measure 10^4 shots of the pulse sequence to ensure the unbiased sampling of all ϕ_p, thereby mitigating its effect. This also demonstrates that the detector can be used for phase-insensitive detection, which is useful when the phase of the signal to be detected is not known or cannot be stabilized with respect to the pump. E is found to grow monotonically with P_0 and is nonzero over a 7-dB range in P_p. For the largest P_0 measured ($P_0 = -111$ dBm), E reaches a maximum of 0.98, which indicates that the device detects the stimulus pulses with high probability and a small number of dark counts. As P_0 is reduced, the P_p at which E is maximized grows slightly (from $P_p = -51.2$ dBm for $P_0 = -111$ dBm to $P_p = -49.4$ dBm for $P_0 = -137$ dBm). This reflects that as P_0 is reduced, the device needs to be biased increasingly closer to P_{th} for successful detection, which results in a corresponding increase to the number of dark counts. In Fig. 3D, we show that the probability of dark counts $P(T|\tilde{S})$ grows from <0.01 to >0.99 over a 3.1-dB range in P_p. This corresponds to a dark count rate that is <0.8 Hz for $P_p < -51.4$ dBm and >23 kHz for $P_p = -48.3$ dBm (see the Supplementary Materials). We note that while we focus here on the setpoint $I_{DC} = 2.0$ mA, the device achieves high E for setpoints between 1.5 and 3.5 mA, corresponding to a tunable bandwidth of ~100 MHz (see the Supplementary Materials).
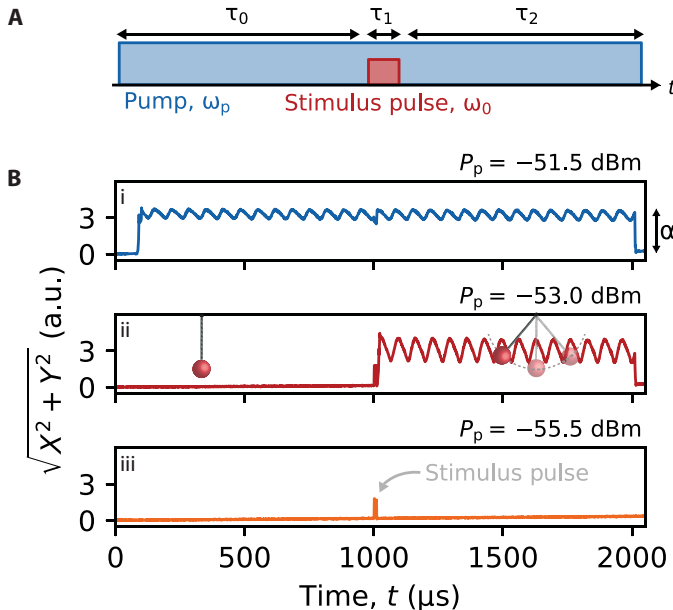

Fig. 2. Detector concept. (**A**) A depiction of the two-tone pulse sequence. The device is biased with I_{DC} and pumped at ω_p, before a short stimulus pulse with frequency ω_0 is supplied to the device. A threshold applied to the amplitude of the demodulated signal is used to determine whether the device is self-oscillating. (**B**) Single shots of the pulse sequence for decreasing P_p (i to iii). For certain P_p, the stimulus pulse triggers the onset of PSO (ii). For these experiments, $\tau_0 = \tau_2 = 1$ ms, $\tau_1 = 10$ μs, $I_{DC} = 2.55$ mA, $P_0 = -116.4$ dBm, and $T = 400$ mK. The time is measured from the leading edge of the pump pulse. The stimulus pulse is seen directly in (iii) at $t = 1000$ μs. a.u., arbitrary units.
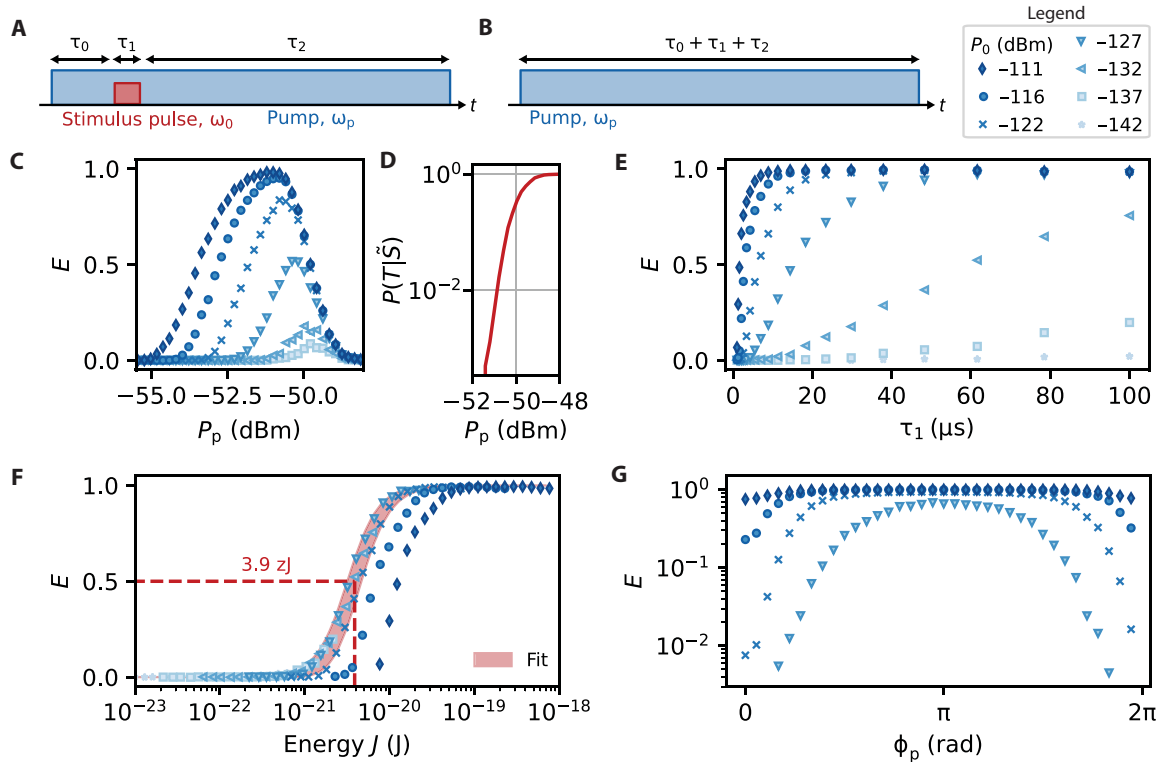
Fig. 3. Detection efficiency measured with calibrated pulses. (**A** and **B**) The experimental pulse sequences used to measure the efficiency of the detector E. The sequence in (B) is a control experiment that measures dark counts. (**C**) E measured as a function of the stimulus pulse power P_0 and pump power P_p. (**D**) The probability of dark counts $P(T|\tilde{S})$ as a function of P_p. (**E**) E measured as a function of P_0 and τ_1 for $P_p = -51.2$ dBm. (**F**) The data in (E) replotted as a function of total wavepacket energy $J = P_0\tau_1$. We determine the lower bound of the detector's sensitivity by fitting the data with $P_0 < -116$ dBm with a sigmoid function (red shaded region). (**G**) E measured as a function of the pump phase ϕ_p with $\tau_1 = 10$ μs. For all experiments, $I_{DC} = 2.0$ mA, $\tau_0 = 10$ μs, $\tau_2 = 100$ μs, and $T = 10$ mK. For each data point, at least 10^4 shots of both the pulse sequences are measured. For all panels, the uncertainties in E are too small to be seen.

Next, we measure the detection efficiency E as a function of the stimulus pulse duration τ_1 (Fig. 3E). We fix the pump power P_p to the value where E was maximized in the previous experiment (-51.2 dBm) and continue to phase modulate the pump. In this experiment, the dark count probability $P(T|\tilde{S})$ is at maximum 1.5×10^{-2}, which ensures that E mainly reflects the probability of true detection $P(T|S)$. E reaches a maximum of $E = 0.995$ and is found to grow monotonically with both P_0 and τ_1. This suggests that E is strongly correlated with the energy of the wavepacket $J = P_0\tau_1$. We confirm this by plotting $E(J)$ (Fig. 3F), where we see that for all P_0, $E(J)$ resembles an activation curve. Fitting the entire dataset with a sigmoid, we infer that $E = 0.5$ for $J = 5.0_{4.0}^{6.3}$ zJ, where the upper and lower bounds correspond to the uncertainty in the calibration of P_0. We note that the E achieved for a given J does show some dependence on P_0, with the two largest P_0 measured having the lowest E. For these two measurements, the cavity ring-down time is as long as $2\omega_0(Q_i^{-1} + Q_c^{-1}) \approx 1.1$ μs, which reduces the detection sensitivity to pulses with short τ_1 at such high powers. This may explain why their activation curves (Fig. 3F) do not align with those taken at lower P_0, where Q_i (and therefore the ring-down time) is reduced. Excluding the data with $P_0 \geq -116$ dBm from the fit (red shaded area in Fig. 3F), we find the lower bound for the sensitivity to be $J = 3.9_{3.1}^{4.9}$ zJ for $E = 0.5$. This corresponds to wavepackets containing 756_{601}^{952} microwave photons, measured at the input of the

device. A complementary method for determining the sensitivity of a detector is plotting the receiver operating characteristic curve (see the Supplementary Materials), where we find that the detector performs better than a random binary classifier for pulse energies above $0.21_{0.17}^{0.27}$ zJ (42_{33}^{52} photons).

Last, we examine the influence of the pump phase ϕ_p on the detection efficiency E by turning off phase modulation on the pump microwave source and instead controlling for and stepping ϕ_p throughout the experiment (Fig. 3G). For each pump power P_p, we found that E could be both enhanced and suppressed by controlling ϕ_p, relative to a control experiment where the pump microwave source was phase modulated. We also found that E averaged across all ϕ_p agreed closely with the efficiency obtained with phase modulation. This confirms for the experiments in Fig. 3 (C to F) that although $1/\tau_1$ is faster than the phase modulation rate, the large number of shots taken ensures that E is independent of ϕ_p when phase modulation is enabled. For $P_0 = -127$ dBm (the weakest power measured in this experiment), E could be suppressed to zero or made as large as 0.68, while with phase modulation, $E = 0.21$. The phase dependence of E highlights that the microwaves absorbed into the resonator are first parametrically amplified and therefore saturate the TLSs more effectively than they would without a strong parametric pump. The sensitivity of the detector can therefore be optimized by operating it in a phase-sensitive manner.

Latched readout of a spin ensemble

Next, we use the device to detect ESR of the ^{209}Bi spin ensemble that was implanted into the Si substrate. At low temperatures, the ^{209}Bi donors bind one extra valence electron compared to the surrounding Si atoms. The bound electron ($S = 1/2$) and nuclear ($I = 9/2$) spins are coupled via the hyperfine interaction $H_A/h = AS \cdot I$, where $A/2\pi = 1.475$ GHz is the hyperfine strength and S and I are the electron and nuclear spin operators, respectively. At fields $B_0 < 100$ mT, the hyperfine interaction strength is comparable to that of the Zeeman interaction $H_B = B_0(\gamma_e S_z - \gamma_n I_z)$, where $\gamma_e/2\pi = 27.997$ GHz/T and $\gamma_n/2\pi = 6.96$ MHz/T are the electron and nuclear spin gyromagnetic ratios, respectively. Under these conditions, the eigenstates of the spin Hamiltonian $H = H_A + H_B$ are best given as F, m_F, where $F = S + I$ is the total spin and m_F is its projection onto B_0. Bismuth donors can have exceptional spin relaxation and coherence times, with $T_1 > 1600$ s (28) and T_2 as long as 700 ms (29), while the large zero-field splitting of the system $5A/2\pi = 7.375$ GHz makes it ideal for applications involving superconducting devices (30, 31).

In our experiments, we apply an in-plane magnetic field of strength $B_0 = 13.71$ mT to bring the $|4, 4\rangle \leftrightarrow |5, 5\rangle$ spin transition into resonance with the device. Resonant pulses delivered to the device are then used to control the sub-ensemble of spins with Larmor frequencies within the bandwidth of the resonator. The spins are measured using a Hahn echo pulse sequence, which is depicted in Fig. 4A. The first pulse in the sequence ($x_{\pi/2}$) is a $\pi/2$ pulse which causes the spins to precess about B_0 and dephase due to interactions with their environment. After a time delay τ_1, a phase-shifted π pulse (y_π) partially reverses the dephasing and causes the spins to refocus and emit an echo, temporarily populating the resonator with photons (32). For the Hahn echo pulse sequence, this refocusing procedure is performed only once, which we designate $N = 1$ (see Fig. 4A).

To detect the spins via PSO, we modify the standard Hahn echo pulse sequence by adding in a strong parametric pump following the refocusing pulse. As in the previous experiments, we set the pump power P_p close to but below the threshold power P_{th}. The spin echo then serves as the stimulus pulse and triggers PSO when it populates the resonator with microwave photons. Individual shots of the pulse sequence are depicted in Fig. 4B. When no pump tone is supplied (blue trace), the device functions simply as a resonator. The first amplifier in the measurement chain is a HEMT at 4 K. As a result, the signal-to-noise ratio (SNR) is poor, and to reliably resolve the echo, the sequence must be repeated so that the signal can be averaged (inset of Fig. 4B). When the pump is on, the echo may trigger PSO, resulting in a detection signal with an amplitude that is a factor ~500 greater than that of the echo (red trace). Moreover, while the echo itself is ≈10 μs long, corresponding to the duration of the resonant pulses used for spin control [as often observed when performing spin resonance on highly coherent spin systems with high-quality factor resonators (12, 15)], the PSO persists until the pump is turned off. This latched ESR readout of a spin ensemble constitutes an original technique for detecting spin resonance.

A common method used to enhance the speed of ESR measurements is to average multiple spin echoes collected with a Carr-Purcell-Meiboom-Gill (CPMG) sequence. The CPMG pulse sequence is an extension of the Hahn-echo pulse sequence that refocuses the spins with y_π pulses a total of N times (Fig. 4A). Neglecting the finite decay of the spin echo throughout the pulse sequence, the SNR of a CPMG measurement is equivalent to that of N Hahn echoes. Notably, however, the amount of measurement time required to achieve a fixed
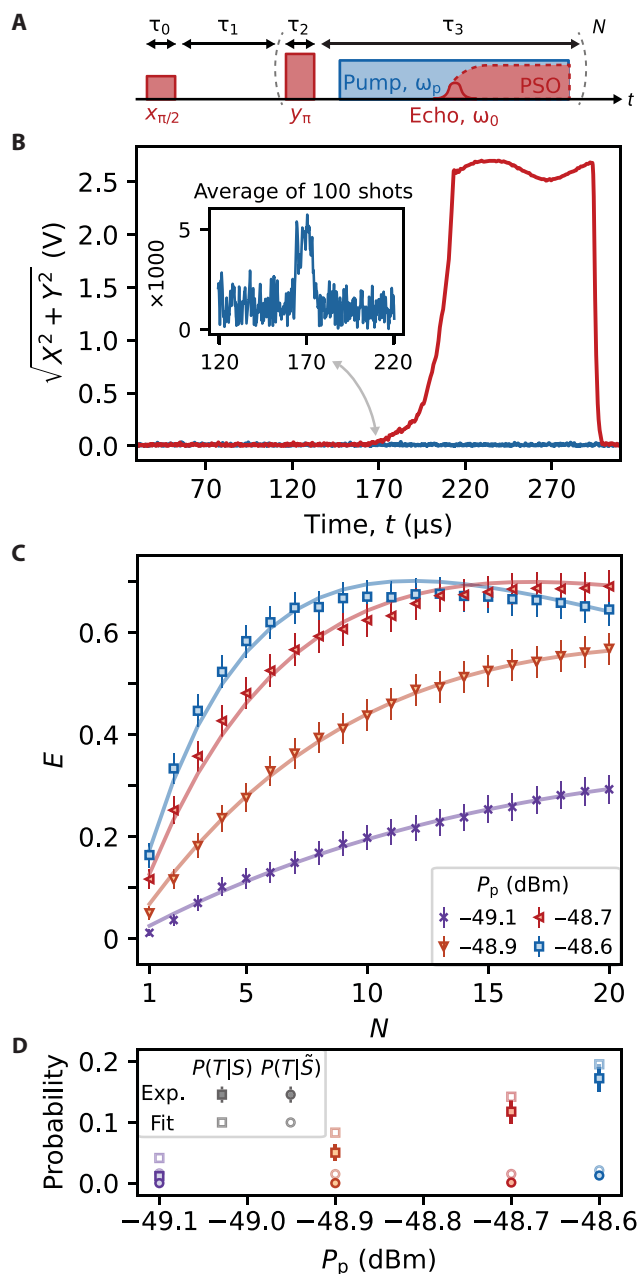

Fig. 4. Latched readout of ^{209}Bi spin echoes. (A) A schematic of the Hahn echo ($N = 1$) and CPMG-N pulse sequences. For the pulses, x and y refer to the phase of the signal while $\pi/2$ and π refer to the tipping angle. When the pump is on, the echo may trigger PSO. $P(T | \tilde{S})$ was measured using sequences where either the $x_{\pi/2}$ or y_π pulses were omitted, so that no spin echo was produced. Both control sequences were performed and resulted in a similar number of dark counts. **(B)** Single shots of the Hahn echo pulse sequence with the pump off (blue) and with with $P_p = -48.6$ dBm (red), measured at a field of $B_0 = 13.71$ mT. Inset: An average of 100 Hahn echoes measured with the pump off—note the scaling of the y axis. The double-sided arrow highlights the correspondence between the time of the spin echo and the onset of PSO. **(C)** E measured as a function of N. For each P_p, a total of 1040 shots of the pulse sequence with $N = 20$ were measured. The errorbars correspond to the 95% confidence interval. The solid lines are fits of the data to Eq. 1. **(D)** A comparison between the experimental values of $P(T|S)$ and $P(T|\tilde{S})$ for $N = 1$ and those fit to the data using Eq. 1. All experiments were completed at $T = 400$ mK with $I_{DC} = 2.55$ mA and with the pump phase modulated at a rate of 15 kHz.

SNR is reduced when using CPMG, because the N echoes are collected within a single shot of the pulse sequence rather than having to wait for the longitudinal magnetization of the spins to recover (in a time T_1) before collecting each echo. In Fig. 4C, we show that this technique can similarly be applied to boost the detection efficiency E of our detector and thereby reduce the amount of measurement time required to detect a spin signal. For each P_p, we perform 1040 shots of the pulse sequence with $N = 20$ refocusing pulses. Because the spins are directly coupled the detector, they are driven by the PSO whenever they are triggered, such that we do not anticipate additional echoes after a detection event. Therefore, we calculate $E(N)$ by determining whether PSO were triggered for any of the N repetitions within each shot of the pulse sequence. We find that by repeatedly refocusing the spin echo, E can be increased by up to a factor of 25 for $P_p = -49.1$ dBm, which, in absolute terms, corresponds to an improvement in E by 0.28. For the three larger values of P_p measured, the absolute improvement to E is even greater, with all being enhanced by more than 0.5 for a modest number of repetitions N.

The CPMG-N experiments can be modeled in a simplified way by treating the detection of each of the N echoes as statistically independent events, with constant probabilities for spin echo detection $P(T|S)$ and dark counts $P(T|\widetilde{S})$. The model therefore assumes that the amplitude of the spin echo does not decay appreciably within the time required to complete the N refocusing pulses. After N echoes, the probability of detecting a spin echo is $1 - [1 - P(T|S)]^N$, and the probability of a dark count is $1 - [1 - P(T|\widetilde{S})]^N$. The efficiency $E(N)$ is their difference and is given by

$$E(N) = [1 - P(T|\widetilde{S})]^N - [1 - P(T|S)]^N \qquad (1)$$

In Fig. 4C, we show that the experimental measurements of $E(N)$ are well-fit by Eq. 1. We also compare the values of the spin echo detection probability $P(T|S)$ and the dark count probability $P(T|\widetilde{S})$ fit to the data with those measured using a Hahn echo sequence ($N = 1$) (Fig. 4D). The general agreement between the two sets of values confirms that the approximation is appropriate for this experiment.

An important consequence of Eq. 1 is that for a CPMG experiment there is a maximum efficiency $E(N)$ and therefore an optimal number of refocusing pulses N. Moreover, this optimal N scales favorably as $\mathcal{O}\left\{\ln[P(T|S) / P(T|\widetilde{S})]\right\}$ (see the Supplementary Materials). We see in Fig. 4C that for $P_p = -48.6$ dBm where $P(T|S) / P(T|\widetilde{S}) = 5.3$, E could be maximized with only $N = 13$ refocusing pulses. This suggests that the CPMG detection scheme should also be effective on spin systems with shorter coherence times, as are commonly found in conventional ESR spectroscopy experiments (33), where the number of refocusing pulses that can be applied is limited. Measuring spins with lower coherence would likely require an increase in both the excitation and detection bandwidth relative to the present device.

DISCUSSION
The sensitivity of the detector could be improved beyond what is demonstrated here by designing a device that is critically coupled ($Q_i = Q_c$), in which case the wavepacket would be more efficiently absorbed by the device. For the current detector, $Q_c/Q_i \approx 24$ for $\overline{n} \approx 1$, in which case the fraction of power that is absorbed is only $1 - |S_{11}|^2 \approx 0.15$. Reducing Q_c to achieve critical coupling, e.g., by modifying the BS-SIF, could therefore increase its sensitivity by nearly an order of

magnitude while simultaneously increasing the bandwidth. We also note that the peak sensitivity was measured in an experiment using phase modulation of the pump microwave source, while in Fig. 3G, we have already demonstrated that E can be increased by more than a factor of three, provided the pump and signal are phase-matched. There may be opportunities to improve the phase-insensitive detection efficiency through optimizing aspects of the pump phase modulation or by considering alternative strategies, such as intentionally detuning the pump frequency.

The sensitivity of future devices could be further enhanced by increasing the strength with which the device couples to TLSs. While this approach is counter to most cQED experiments, in the present case, it will increase the sensitivity of Q_i to the average number of intracavity photons $\overline{n}$, which is central to signal detection. This could be achieved by reducing the widths of the coplanar waveguide gap (g) and conductor (w) below the dimensions of the present device ($g = 1.5$ μm, $w = 1$ μm). Because TLSs reside at the dielectric interface, this will have the effect of concentrating the resonant mode volume in the material hosting the TLSs (27, 34). In addition, dielectrics with higher concentrations of TLSs (35–37) could be intentionally deposited to improve both the detection sensitivity and bandwidth. If the sensitivity can be improved to the single photon level, the KIPO could be used as a detector of itinerant microwave photons, which might make it applicable in schemes for generating remote entanglement between qubits (38) or nonclassical states of light (39).

The experiments presented in Fig. 4 are a proof of concept that demonstrate how the detector might be used in ESR experiments. While the experiments in Fig. 4 are taken at a single magnetic field B_0, we also compare the conventional ESR and KIPO methods over a range of B_0 fields, simulating how the KIPO might be used as a spectroscopic probe (see the Supplementary Materials). This experiment further highlights that while detection of the spin echoes with the KIPO occurs with probability <1, the KIPO signal is greater than conventional ESR methods even when averaging over all shots and accounting for dark counts. This is directly related to the large power of the PSO signal, which we show in Fig. 1C can exceed −75 dBm at its peak, referred to the output of the device. This is ∼20 dB greater than the equivalent room temperature Johnson-Nyquist noise measured over a bandwidth of 100 MHz, which means that it would be possible to measure "clicks" produced by the KIPO even without a cryogenic HEMT amplifier.

The experiments shown in Fig. 4, (C and D) show that ESR detection using the KIPO benefits from the extension of conventional ESR techniques. Further, it was recently demonstrated how click detectors can be used to perform a full suite of ESR techniques (19), which may be similarly adapted to the KIPO. Continuous-wave ESR detection might also be explored, as demonstrated using classical oscillator circuits that operate deep in the oscillator regime (40). In comparing the KIPO to works using Josephson junction–based devices, we emphasize the simplicity of our experiment. The KIPO does not require any qubits for detecting the microwave signals and can be operated at elevated temperatures and directly in a magnetic field (here 400 mK and 13.71 mT, which would preclude the use of aluminum Josephson junctions). Ultimately, this enables the KIPO to be coupled directly to the spin ensemble, which obviates a following quantum-limited amplifier or a cryogenic HEMT amplifier, as noted above. Future work will focus on comparing both detection techniques and further exploring the advantages of latched echo readout in ESR spectroscopy.

MATERIALS AND METHODS

Device fabrication

The silicon substrate is enriched in the isotope ^{28}Si with a residual ^{29}Si concentration of 750 ppm. ^{209}Bi ions with multiple energies were implanted to a concentration of 10^{17} cm^{-3} between 0.75- and 1.75-μm depth and electrically activated with a 20-min anneal at 800°C in a N$_2$ environment. A 50-nm film of NbTiN was then sputtered (STAR Cryoelectronics). The film was determined to have a kinetic inductance of 3.45 pH/□ by matching the resonant frequencies of capacitively coupled λ/4 resonators to microwave simulations (Sonnet). The device was patterned in a single step with electron beam lithography and subsequently dry-etched with a CF$_4$/Ar plasma. The device was then mounted and wire bonded to a printed circuit board and enclosed in a three-dimensional copper cavity.

Measurement setups

The measurements are performed in two different cryogenic systems: a dry dilution refrigerator with a base temperature of 10 mK and a pumped ^{3}He cryostat with a base temperature of 400 mK. In both setups, DC and microwave signals are combined at the coldest stage with a bias-tee and diplexer, and two cryogenic circulators are used to route the reflected microwave signals to cryogenic HEMT amplifiers. For the ESR measurements performed in the ^{3}He refrigerator, a solenoid is used to generate the B_0 field. The cryogenic circulators are placed outside of the magnet bore and contain two layers of magnetic shielding to protect them from any stray magnetic fields. In some experiments, additional amplification and filtering of the microwave and baseband signals are performed at room temperature. Time resolved measurements are performed via homodyne detection with $\omega_{LO} = \omega_p/2$ using a homemade microwave bridge. The Supplementary Materials includes detailed schematics of both setups.

VNA measurements

VNA measurements were fit to cavity input-output theory (41) to extract ω_0, Q_i, and Q_c. For the data in Fig. 1D, a baseline was measured and subtracted from each measurement, by setting $I_{DC} = 0$ mA, which shifted ω_0 outside the measurement window.

Measurement of E

The measurements of E presented in Fig. 3 were collected by repeating each pulse sequence 500 shots at a time, with a 33-Hz repetition rate (pump duty cycle $\approx 1/250$). In each experiment, the parameters being swept (P_0, P_p, τ_1, ϕ_p, and the corresponding control experiments) were selected in pseudo-random order. For each datapoint, a minimum of 10^4 shots of both the experimental and control sequences were run. A threshold applied to the amplitude of the demodulated signal $\sqrt{X^2 + Y^2}$ was used to determine whether the device self-oscillated. For the experiments in Fig. 3 (A to D), the pump was phase-modulated at a rate of 15 kHz to ensure that E would not be dependent on ϕ_p. In Fig. 3E, phase modulation was disabled. Despite a 3-GHz clock used to sync the two microwave sources, a small phase drift was still evident in $P(T|S)$ [the control experiments used for calculating $P(T|\widetilde{S})$ showed no trend, as expected]. To correct for the phase drift, $P(T|S)$ for each experimental repetition (500 shots for each ϕ_p) was fit with a phenomenological function and aligned with the minimum E on $\phi_p = 0$. For all measurements of E, the uncertainties were found by adding in quadrature the 95% confidence intervals for the binomial distributions of $P(T|S)$ and $P(T|\widetilde{S})$.

Measurements of ^{209}Bi

All measurements of ^{209}Bi were performed at 400 mK. The device is mounted so that B_0 is aligned parallel to the long axis of the resonator. This orientation is chosen so that the magnetic field of the resonant mode B_1 is perpendicular to B_0 for spins located underneath the resonator. Numerically solving the ^{209}Bi spin Hamiltonian allows one to target specific ^{209}Bi ESR transitions by adjusting B_0 until the spins are resonant with the cavity. In this work, we measure the $|4, 4\rangle \leftrightarrow |5, 5\rangle$ spin transition. The small discrepancy between the B_0 at which we measure ESR (13.71 mT) and the numerically predicted field (13.54 mT) might be attributed to strain caused by the different coefficients of thermal expansion of the Si substrate and NbTiN thin film (42) or a slight miscalibration of the superconducting solenoid used to generate B_0. For the Hahn echo and CMPG sequences used for the experiments in Fig. 4, we use $\tau_0 = \tau_2 = 10$ μs, $\tau_1 = 150$ μs, and $\tau_3 = 2\tau_1 + 4\tau_0/\pi$ (43). The leading edge and trailing edges of the pump pulses are padded by 50 and 30 μs with respect to the π_y pulses, to avoid their amplification. The sequences were measured with a repetition time of 7 s. This is similar in magnitude to the spin relaxation rate $T_1 \approx 12$ s, which, in our experiments, is limited by spin diffusion (12). For the experiment in Fig. 4C, a total of 1040 shots of the full sequence with $N = 20$ were measured for both the control and experimental sequences at each P_p while alternating between the control and experimental sequences. We performed two independent control sequences: one where the $x_{\pi/2}$ pulse was excluded and a second where the twenty y_π pulses were excluded. The two values of $P(T|\widetilde{S})$ were found to agree closely with one another, despite the different timing of the pulses relative to the onset of the pump. This indicates that the dark count rate was not influenced by residual fields of the $x_{\pi/2}$ and y_π pulses in this experiment. Histograms of the detector counts for the experimental and control sequences as a function of time and repetition N are provided in the Supplementary Materials.

Calibration of powers

All powers mentioned throughout the text are referred to the input of the device enclosure. To calibrate these powers, we performed three separate cooldowns of the cryostats with two additional high-frequency lines (L_1 and L_2). In the first two cooldowns, L_1 or L_2 was connected in place of the device, and S_{21} measurements of each pair of lines were taken. In the third cooldown, an S_{21} measurement was taken where L_1 and L_2 were connected to one another at the base temperature plate. The combination of S_{21} measurements taken over the three cooldowns allowed for a full reconstruction of the gain (loss) of each line, which agreed closely with the designed amplification (attenuation). We estimate the powers to be accurate to within ± 1 dB.

Supplementary Materials

This PDF file includes:
Supplementary text
Figs. S1 to S14
Table S1
References

REFERENCES AND NOTES

1. I. Siddiqi, R. Vijay, F. Pierre, C. M. Wilson, M. Metcalfe, C. Rigetti, L. Frunzio, M. H. Devoret, RFdriven Josephson bifurcation amplifier for quantum measurement. *Phys. Rev. Lett.* **93**, 207002 (2004).

2. Z. R. Lin, K. Inomata, K. Koshino, W. D. Oliver, Y. Nakamura, J. S. Tsai, T. Yamamoto, Josephson parametric phase-locked oscillator and its application to dispersive readout of superconducting qubits. *Nat. Commun.* **5**, 4480 (2014).

3. P. Krantz, A. Bengtsson, M. Simoen, S. Gustavsson, V. Shumeiko, W. D. Oliver, C. M. Wilson, P. Delsing, J. Bylander, Single-shot read-out of a superconducting qubit using a Josephson parametric oscillator. *Nat. Commun.* **7**, 11417 (2016).

4. K. Petrovnin, J. Wang, M. Perelshtein, P. Hakonen, G. S. Paraoanu, Microwave photon detection at parametric criticality. *arXiv*. 2308.07084. (2023).

5. B. H. Eom, P. K. Day, H. G. Le Duc, J. Zmuidzinas, A wideband, low-noise superconducting amplifier with high dynamic range. *Nat. Phys.* **8**, 623–627 (2012).

6. N. Samkharadze, A. Bruno, P. Scarlino, G. Zheng, D. P. Di Vincenzo, L. Di Carlo, L. M. K. Vandersypen, High-kinetic-inductance superconducting nanowire resonators for circuit QED in a magnetic field. *Phys. Rev. Appl.* **5**, 044004 (2016).

7. J. G. Kroll, F. Borsoi, K. L. van der Enden, W. Uilhoorn, D. de Jong, M. Quintero-Pérez, D. J. van Woerkom, A. Bruno, S. R. Plissard, D. Car, E. P. A. M. Bakkers, M. C. Cassidy, L. P. Kouwenhoven, Magnetic-Field-Resilient superconducting coplanar-waveguide resonators for hybrid circuit quantum electrodynamics experiments. *Phys. Rev. Applied* **11**, 064053 (2019).

8. A. Vaartjes, A. Kringhøj, W. Vine, T. Day, A. Morello, J. J. Pla, Strong microwave squeezing above 1 tesla and 1 kelvin. *arXiv*. 2311.07968. (2023).

9. D. J. Parker, M. Savytskyi, W. Vine, A. Laucht, T. Duty, A. Morello, A. L. Grimsmo, J. J. Pla, Degenerate parametric amplification via three-wave mixing using kinetic inductance. *Phys. Rev. Applied* **17**, 034064 (2022).

10. M. Xu, R. Cheng, Y. Wu, G. Liu, H. X. Tang, Magnetic field-resilient quantum-limited parametric amplifier. *PRX Quantum* **4**, 010322 (2023).

11. M. Khalifa, J. Salfi, Nonlinearity and parametric amplification of superconducting nanowire resonators in magnetic field. *Phys. Rev. Applied* **19**, 034024 (2023).

12. W. Vine, M. Savytskyi, A. Vaartjes, A. Kringhøj, D. Parker, J. Slack-Smith, T. Schenkel, K. Mølmer, J. C. M. Callum, B. C. Johnson, A. Morello, J. J. Pla *et al.*, *Sci Adv* **9**, adg1593 (2023).

13. K. M. Backes, D. A. Palken, S. A. Kenany, B. M. Brubaker, S. B. Cahn, A. Droster, G. C. Hilton, S. Ghosh, H. Jackson, S. K. Lamoreaux, A. F. Leder, K. W. Lehnert, S. M. Lewis, M. Malnou, R. H. Maruyama, N. M. Rapidis, M. Simanovskaia, S. Singh, D. H. Speller, I. Urdinaran, L. R. Vale, E. C. van Assendelft, K. van Bibber, H. Wang, A quantum-enhanced search for dark matter axions. *Nature* **590**, 238–242 (2021).

14. G. A. Oakes, V. N. Ciriano-Tejel, D. F. Wise, M. A. Fogarty, T. Lundberg, C. Lainé, S. Schaal, F. Martins, D. J. Ibberson, L. Hutin, B. Bertrand, N. Stelmashenko, J. W. A. Robinson, L. Ibberson, A. Hashim, I. Siddiqi, A. Lee, M. Vinet, C. G. Smith, J. J. L. Morton, M. F. Gonzalez-Zalba, Fast high-fidelity single-shot readout of spins in silicon using a single-electron box. *Phys. Rev. X* **13**, 011023 (2023).

15. A. Bienfait, J. J. Pla, Y. Kubo, X. Zhou, M. Stern, C. C. Lo, C. D. Weis, T. Schenkel, M. L. W. Thewalt, D. Vion, D. Esteve, B. Julsgaard, K. Mølmer, J. J. L. Morton, P. Bertet, Reaching the quantum limit of sensitivity in electron spin resonance. *Nat. Nanotechnol.* **11**, 253–257 (2016).

16. C. Eichler, A. J. Sigillito, S. A. Lyon, J. R. Petta, Electron spin resonance at the level of 10^4 spins using low impedance superconducting resonators. *Phys. Rev. Lett.* **118**, 037701 (2017).

17. R. P. Budoyo, K. Kakuyanagi, H. Toida, Y. Matsuzaki, W. J. Munro, H. Yamaguchi, S. Saito, Electron paramagnetic resonance spectroscopy of $Er^{3+}:Y_2SiO_5$ using a Josephson bifurcation amplifier: Observation of hyperfine and quadrupole structures. *Phys. Rev. Materials* **2**, 011403 (2018).

18. R. P. Budoyo, K. Kakuyanagi, H. Toida, Y. Matsuzaki, S. Saito, Electron spin resonance with up to 20 spin sensitivity measured using a superconducting flux qubit. *Appl. Phys. Lett.* **116**, 194001 (2020).

19. E. Albertinale, L. Balembois, E. Billaud, V. Ranjan, D. Flanigan, T. Schenkel, D. Estève, D. Vion, P. Bertet, E. Flurin, Detecting spins by their fluorescence with a microwave photon counter. *Nature* **600**, 434–438 (2021).

20. E. Billaud, L. Balembois, M. L. Dantec, M. Rančić, E. Albertinale, S. Bertaina, T. Chanelière, P. Goldner, D. Estève, D. Vion, P. Bertet, E. Flurin, Microwave fluorescence detection of spin echoes. *arXiv*. 2208.13586 (2022).

21. Z. Wang, L. Balembois, M. Rančić, E. Billaud, M. le Dantec, A. Ferrier, P. Goldner, S. Bertaina, T. Chanelière, D. Esteve, D. Vion, P. Bertet, E. Flurin, Single-electron spin resonance detection by microwave photon counting. *Nature* **619**, 276–281 (2023).

22. N. T. Bronn, Y. Liu, J. B. Hertzberg, A. D. Córcoles, A. A. Houck, J. M. Gambetta, J. M. Chow, Broadband filters for abatement of spontaneous emission in circuit quantum electrodynamics. *Appl. Phys. Lett.* **107**, 172601 (2015).

23. A. T. Asfaw, A. J. Sigillito, A. M. Tyryshkin, T. Schenkel, S. A. Lyon, Multi-frequency spin manipulation using rapidly tunable superconducting coplanarwaveguide microresonators. *Appl. Phys. Lett.* **111**, 032601 (2017).

24. M. R. Vissers, R. P. Erickson, H. S. Ku, L. Vale, X. Wu, G. C. Hilton, D. P. Pappas, Low-noise kinetic inductance traveling-wave amplifier using three-wave mixing. *Appl. Phys. Lett.* **108**, 012601 (2016).

25. C. M. Wilson, T. Duty, M. Sandberg, F. Persson, V. Shumeiko, P. Delsing, Photon generation in an electromagnetic cavity with a time-dependent boundary. *Phys. Rev. Lett.* **105**, 233907 (2010).

26. W. Wustmann, V. Shumeiko, Parametric resonance in tunable superconducting cavities. *Phys. Rev. B* **87**, 184501 (2013).

27. H. Wang, J. Gao, M. R. Vissers, T. Brecht, A. Dunsworth, D. P. Pappas, J. Mutus, Materials loss measurements using superconducting microwave resonators. *Rev. Sci. Instrum.* **91**, 091101 (2020).

28. A. Bienfait, J. J. Pla, Y. Kubo, X. Zhou, M. Stern, C. C. Lo, C. D. Weis, T. Schenkel, D. Vion, D. Esteve, J. J. L. Morton, P. Bertet, Controlling spin relaxation with a cavity. *Nature* **531**, 74–77 (2016).

29. G. Wolfowicz, S. Simmons, A. M. Tyryshkin, R. E. George, H. Riemann, N. V. Abrosimov, P. Becker, H.-J. Pohl, S. A. Lyon, M. L. W. Thewalt, J. J. L. Morton, Decoherence mechanisms of ^{209}Bi donor electron spins in isotopically pure ^{28}Si. *Phys. Rev. B* **86**, 245301 (2012).

30. V. Ranjan, J. O'Sullivan, E. Albertinale, B. Albanese, T. Chanelière, T. Schenkel, D. Vion, D. Esteve, E. Flurin, J. J. L. Morton, P. Bertet, Multimode storage of quantum microwave fields in electron spins over 100 ms. *Phys. Rev. Lett.* **125**, 210505 (2020).

31. J. O'Sullivan *et al.*, Random-access quantum memory using chirped pulse phase encoding. *Phys. Rev. X* **12**, 041014 (2022).

32. J. J. L. Morton, P. Bertet, Storing quantum information in spins and high-sensitivity ESR. *J. Magn. Reson.* **287**, 128–139 (2018).

33. L. J. Berliner, G. R. Eaton, S. S. Eaton, Distance Measurements in Biological Systems by EPR. Springer Science & Business Media, 2006.

34. D. Niepce, J. J. Burnett, M. G. Latorre, J. Bylander, Geometric scaling of two-level-system loss in superconducting resonators. *Supercond. Sci. Technol.* **33**, 025013 (2020).

35. J. M. Martinis, K. B. Cooper, R. M. Dermott, M. Steffen, M. Ansmann, K. D. Osborn, K. Cicak, S. Oh, D. P. Pappas, R. W. Simmonds, C. C. Yu, Decoherence in Josephson qubits from dielectric Loss. *Phys. Rev. Lett.* **95**, 210503 (2005).

36. J. Gao, M. Daal, A. Vayonakis, S. Kumar, J. Zmuidzinas, B. Sadoulet, B. A. Mazin, P. K. Day, H. G. Leduc, Experimental evidence for a surface distribution of two-level systems in superconducting lithographed microwave resonators. *Appl. Phys. Lett.* **92**, 152505 (2008).

37. J. H. Ungerer, D. Sarmah, A. Kononov, J. Ridderbos, R. Haller, L. Y. Cheung, C. Schönenberger, Performance of high impedance resonators in dirty dielectric environments. *EPJ Quantum Technol.* **10**, 41 (2023).

38. P. C. Humphreys, N. Kalb, J. P. J. Morits, R. N. Schouten, R. F. L. Vermeulen, D. J. Twitchen, M. Markham, R. Hanson, Deterministic delivery of remote entanglement on a quantum network. *Nature* **558**, 268–273 (2018).

39. A. Ourjoumtsev, R. Tualle-Brouri, J. Laurat, P. Grangier, Generating optical Schrödinger kittens for quantum information processing. *Science* **312**, 83–86 (2006).

40. J. Anders, A. Angerhofer, G. Boero *et al.*, *J. Magn. Reson.* **217**, 19–26 (2012).

41. S. Probst, F. B. Song, P. A. Bushev, A. V. Ustinov, M. Weides, Efficient and robust analysis of complex scattering data under noise in microwave resonators. *Rev. Sci. Instrum.* **86**, 024706 (2015).

42. J. J. Pla, A. Bienfait, G. Pica, J. Mansir, F. A. Mohiyaddin, Z. Zeng, Y. M. Niquet, A. Morello, T. Schenkel, J. J. L. Morton, P. Bertet, Strain-induced spin-resonance shifts in silicon devices. *Phys. Rev. Applied* **9**, 044014 (2018).

43. C. P. Slichter, *Princples of Magnetic Resonance* (Springer, Berlin, ed. 3, 1996).

44. M. R. Vissers, J. Hubmayr, M. Sandberg, S. Chaudhuri, C. Bockstiegel, J. Gao, Frequency-tunable superconducting resonators via nonlinear kinetic inductance. *Appl. Phys. Lett.* **107**, 062601 (2015).

45. A. Bruno, G. de Lange, S. Asaad, K. L. van der Enden, N. K. Langford, L. DiCarlo, Reducing intrinsic loss in superconducting resonators by surface treatment and deep etching of silicon substrates. *Appl. Phys. Lett.* **106**, 182601 (2015).

46. D. Niepce, J. Burnett, J. Bylander, High kinetic inductance NbN nanowire superinductors. *Phys. Rev. Applied* **11**, 044014 (2019).

47. R. P. Erickson, M. R. Vissers, M. Sandberg, S. R. Jefferts, D. P. Pappas, Frequency comb generation in superconducting resonators. *Phys. Rev. Lett.* **113**, 187002 (2014).

48. M. C. Cassidy, A. Bruno, S. Rubbert, M. Irfan, J. Kammhuber, R. N. Schouten, A. R. Akhmerov, L. P. Kouwenhoven, Demonstration of an ac Josephson junction laser. *Science* **355**, 939–942 (2017).

49. S. Khan, H. E. Türeci, Frequency combs in a lumped-element josephson-junction circuit. *Phys. Rev. Lett.* **120**, 153601 (2018).

50. P. Lu, T.-C. Chien, X. Cao, O. Lanes, C. Zhou, M. J. Hatridge, S. Khan, H. E. Türeci, Nearly quantum-limited Josephson junction frequency-comb synthesizer. *Phys. Rev. Applied* **15**, 044031 (2021).

51. S. P. Wang, Z. Chen, T. Li, Control lable microwave frequency comb generation in a tunable superconducting coplanar-waveguide resonator. *Chinese Phys. B* **30**, 048501 (2021).

52. J. Y. Qiu, A. Grimsmo, K. Peng, B. Kannan, B. Lienhard, Y. Sung, P. Krantz, V. Bolkhovsky, G. Calusine, D. Kim, A. Melville, B. M. Niedzielski, J. Yoder, M. E. Schwartz, T. P. Orlando, I. Siddiqi, S. Gustavsson, K. P. O'Brien, W. D. Oliver, Broadband squeezed microwaves and

amplification with a Josephson travelling-wave parametric amplifier. *Nat. Phys.* **19**, 706–713 (2023).